Supplementary Information

Microstructural Metrology of Tobacco Mosaic Virus Nanorods during Radial Compression and Heating

Christian Riekel[*], *Manfred Burghammer, Irina Snigirev and Martin Rosenthal*

The European Synchrotron, ESRF, CS40220, F-38043 Grenoble Cedex 9, France

Materials. TMV capsids were purified from infected tobacco leaves of *Nicotiana tabacum var. Samsun* using differential centrifugations[1, 2]. Purified capsids (4.41 µM) were conserved in EDTA 1 mM, pH 7.7, at 4°C. 10 µl of 405 µg/mL were diluted with 100 µL deionized water.

Coffee-Ring Structure Generation. 1-3 µL droplets corresponding to 40 µg/µL capsids were deposited by a pipette on wetting Si_3N_4 membranes. We deposited the droplets on a Silson Ltd chip composed of a Si_3N_4 membrane and surrounding silicon supporting frame so that part of the approximately circular coffee-ring was on the membrane and part on the frame (Figure 1A). Higher resolution optical images of the air-dry coffee-ring structure (not shown) reveal the same crack-morphology as the SEM image of the vacuum-dried coffee-ring structure (Figure 1B). To position a segment of the coffee-ring within the 100x100 μm^2 active area of the Si_3N_4 membrane of the nanocalorimeter we displaced the droplet rim manually with the pipette-tip resulting in racetrack shapes (Figure 1C). This approach is limited to about 1 µL droplets minimum volume while high heating rate nanocalorimetry experiments >1000K/s require the deposition of smaller sample quantities on the active area[3, 4]. Indeed, a coffee-ring structure corresponding to 0.07 µg TMV capsids could be generated

by depositing an 18 nL droplet of a 4 μg/μL TMV sol by a nanodrop dispensing system on the nanocalorimeter window (Figure S1). The average diameter of the coffee-ring structure in Figure S1 is 314 μm. Smaller coffee-ring structures could be generated by depositing sub-nL droplets by an inkjet system[5]. The minimum diameter of a coffee-ring structure attainable has been estimated as 10 μm[6].

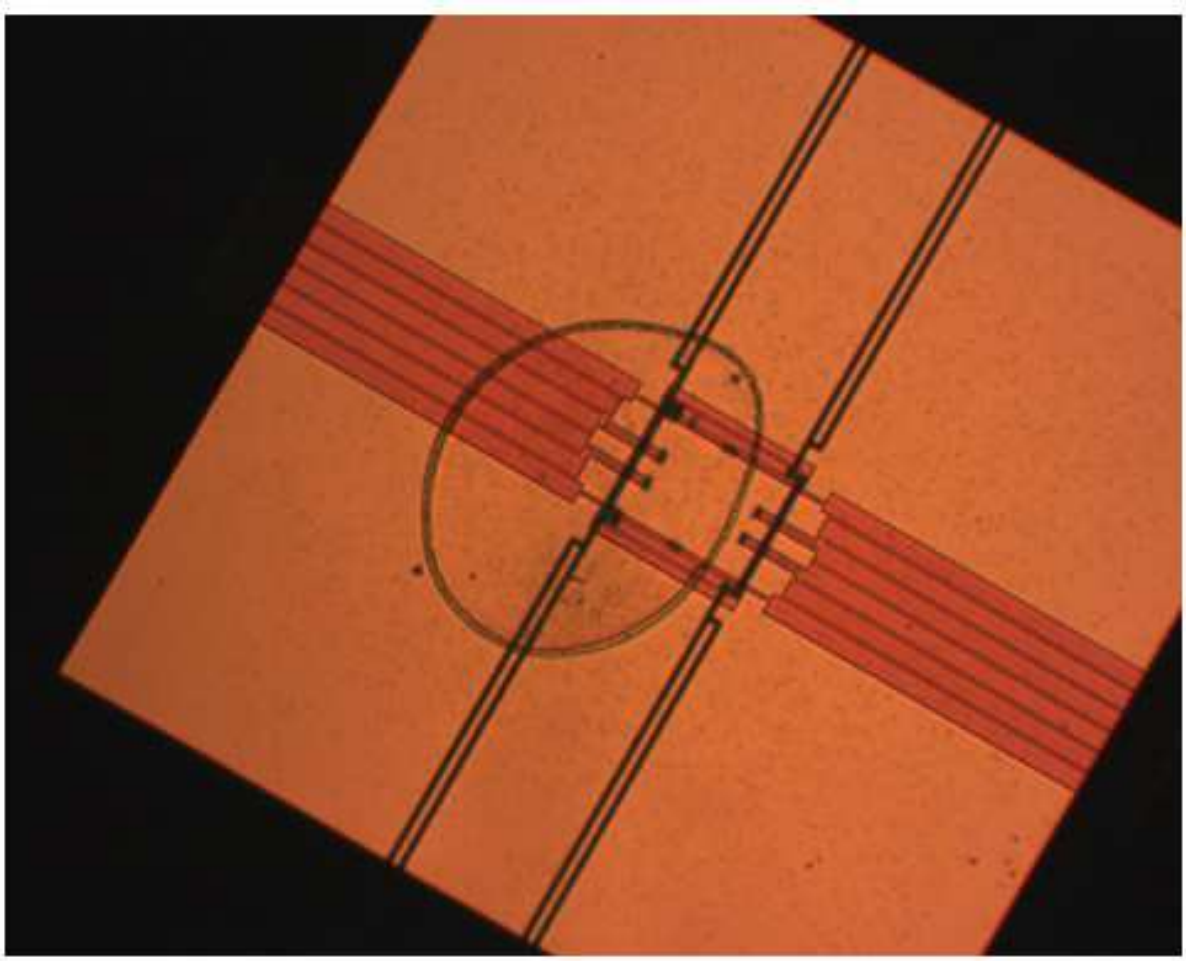

Figure S1: Coffee-ring structure generated from 18 nL droplet of 4 mg/ml capsids sol on a nanocalorimeter chip. The chip dimensions correspond to Figure 1C.

Synchrotron Radiation (SR) Experiments. SR-experiments were performed at the ID13 beamline of "The European Synchrotron (ESRF)" in transmission geometry with the X-ray beam approximately normal to the Si_3N_4 membrane surface of the nanocalorimeter[8]. A monochromatic beam with $\Delta\lambda/\lambda \sim 2*10^{-4}$ was obtained from the pink beam of an undulator source by a double Si crystal. Nanobeam X-ray diffraction (nanoXRD) experiments were

performed with λ=0.0835 and 0.847 nm beams, focused to about 150-200 nm spots in horizontal and vertical directions at the sample position by Si refractive lenses in crossed geometry[9]. Typical experiments were performed with a flux in the focal spot of $\Phi \sim 8.3 \times 10^9$ photons s^{-1} (at 200 mA) corresponding to a flux density of $\Phi_d \sim 3.5 \times 10^5$ photons s^{-1} nm^{-2}.

An inverted Olympus microscope with reflected light illumination was used for sample alignment in the SR beam. The coffee-ring structures were step-scanned through the focus by a piezoelectric actuator stack along the orthogonal horizontal (y) and vertical (z) axes. We used a FRELON detector system based on a CCD camera with X-ray converter screen and relay optics (2Kx2K pixels, 16-bit readout with 2x2 binning)[10] or an EIGER 4M pixel detector (Dectris®) with 2070x2167 pixels and single photon counting capability at a framing rate of about 300 Hz[9]. We performed two mesh-scans at room temperature (r.t.) with the coffee-ring structure on a Silson Ltd chip and two series of linear scans across the coffee-ring structure on the nanocalorimeter membrane with step-wise increase of the temperature. The scan parameters are indicated in Table S1.

Table S1 Parameters of raster-scans performed

Scan	type	detector	detector-sample (mm)	step-increment (μm)	temperature - T (°C)
SC1	1D	pixel	447.7	1	r.t. to 135 with ΔT=10 °C then 150/200/250 °C
SC2	1D	CCD	265.1	1	fast step to 140 °C then 140 to 225 °C with ΔT=5 °C
M1	2D	pixel	253.6	1x1	r.t.

Data Reduction and Analysis. Analysis and display of patterns was performed by FIT2D[11]. We used Origin® for plotting intensity profiles and peak fit parameters. The patterns recorded

by the pixel detector were analyzed without distortion correction. Intensities were obtained using FIT2D by masking non-sensitive areas on the detector. The patterns recorded by the CCD system were corrected for dark field effects and geometrical distortions due to the X-ray conversion/relay system. The exposure time per pattern was adjusted to limit radiation damage affecting reflection intensities. A pattern recorded with the beam outside the sample but within the sample support was subtracted for background correction.

Calibration Procedures. Detector distances and the orientation of the detector were calibrated for nanoXRD by a silver-behenate standard (Rose Chemical Ltd; Batch 2301) which has a 1st order lamellar spacing of 5.837 nm[12]. The position of the beam on the detector and the tilting of the detector plane from normal beam incidence were determined from the (00l) reflections of selected Ag-behenate crystallites recorded during a mesh-scan. We determined the peak positions and peak width by fitting Gaussian profiles using FIT2D[11]. Indeed, the variation of the peak width with Q is shown in Figure S2B. The sample-to-detector distances for the different nanoXRD scans collected in Table S1 were determined by averaging the distance values obtained from the silver-behenate orders. SEM images of behenate crystallites reveal an inhomogeneous particle size (Figure S2C). We performed therefore complementary experiments on an Al_2O_3 powder standard (NBS: SRM 674a) which reveals a more homogeneous particle size distribution in an SEM image (Figure S2D). Mesh-scans were performed with a larger beam of $3_{hor}x2_{ver}$ μm^2 beam of λ=0.0954 nm. The variation of the peak width with Q is shown in Figure 2E. We calculate an average particle size of 58 nm at Q~20 nm^{-1}. The Figure contains also values for the Bragg peaks on the equator and the layer-lines of a single pattern from the outer domain boundary shown in Figure 2F.

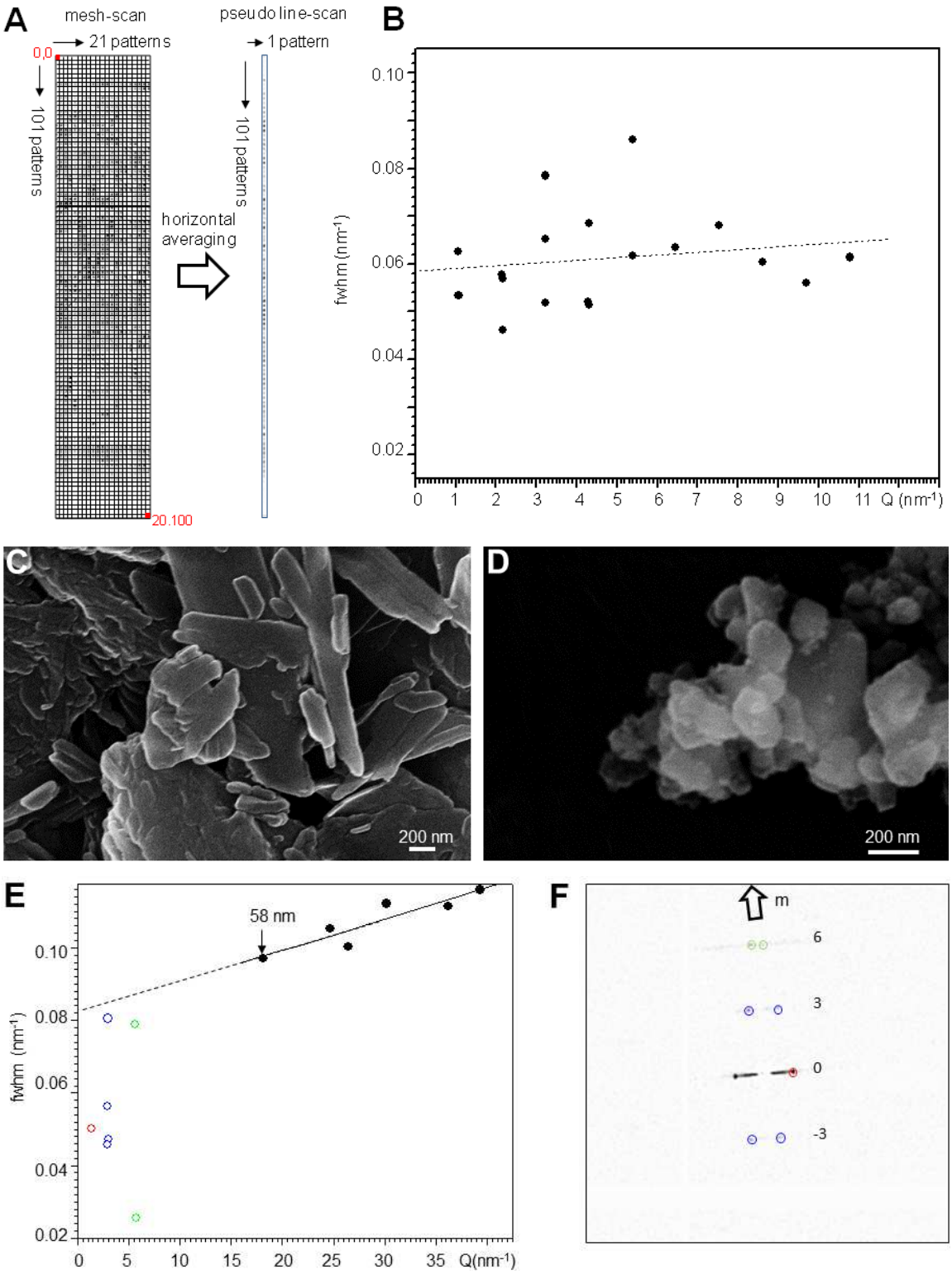

Figure S2 A: Generation of $1_{hor}x21_{ver}$ pixels pseudo line-scan by averaging each horizontal line of 21 pixels of a $21_{hor}x101_{ver}$ pixels mesh-scan. **B**: Variation of Gaussian peak width (fwhm) of (00l) reflections from single Ag-behenate crystallites. A linear regression curves was fitted as a guide-to-the-eye **C**: SEM image of Ag-behenate crystallites. **D**: SEM image of Al_2O_3 crystallites. **E**: Gaussian width (fwhm) of Al_2O_3 powder rings (solid circles) and of TMV Bragg peaks on layer-lines -3, 0, 3, 6 (open circles). The fluctuations of the TMV data are probably due to the difficulty in separating helical scattering from the weaker Bragg peaks. The Al_2O_3 particles size has been calculated using Scherrer's equation.[13] A linear regression curve was fitted as a guide-to-the-eye to the $A_{l2}O_3$ data and extrapolated to the TMV data. **F**: Single TMV pattern obtained by microXRD in outer boundary zone. The peaks used in (F) have been mapped by rings with the same colours.

Determination of Helical Repeat. The helical repeat was determined from the average of the distances of the two opposite 3rd layer-lines from the centre of the pattern. For the TMV clusters observed in the bulk of the residue (Z_3-zone) we observed few peaks and used also the diffuse scattering on the layer-lines. The radial position was determined for the azimuthally averaged pattern by a Gaussian fit. For the hexagonal and tetragonal phases we used reflections on the 3rd layer-line which closest to the meridian (Figure S3A). In view of the dependence of the layer-line spacing on the probing position in the residue (Figure 3A) we determined the helical repeats for the heating experiments shown in Figure 11A in the outer boundary zone of the residue. Patterns from the outer boundary zone were also used to determine the (100) lattice spacing in Figure 10B (Figure S3 C,D).

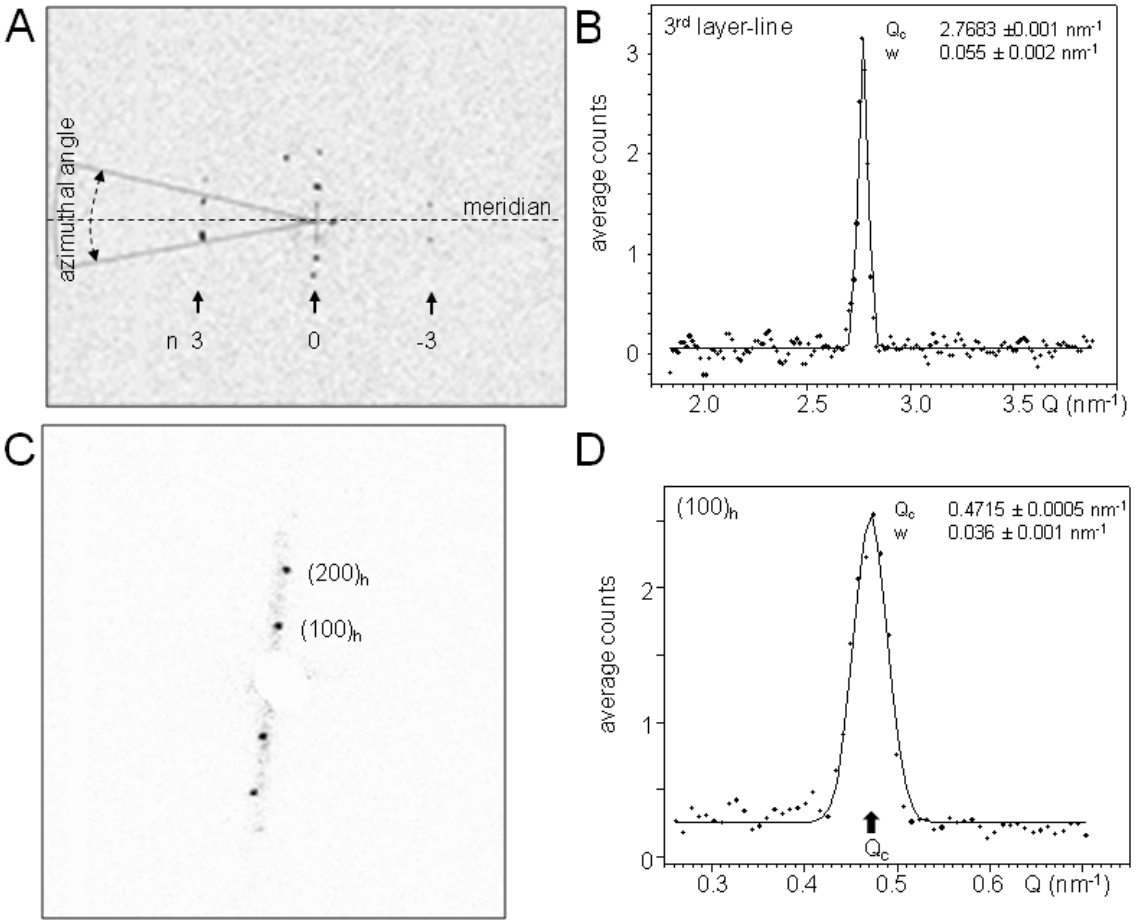

Figure S3 A: Pattern showing equator (n=0) and 3rd layer-lines (n=3/-3) of the hexagonal phase. The 3rd layer-line reflections were azimuthally averaged within the angular range indicated. **B**: Radial intensity profile of 3rd layer-line fitted by a Gaussian for the Bragg reflection. The Gaussian profile parameters: peak position (Q_c) and width (w; σ) are indicated. **C**: Pattern showing the equatorial trace with $(100)_h$ and $(200)_h$ reflections. **D**: Gaussian fit to $(100)_h$ reflection radial intensity profile.

Heat Maps. The heat maps shown in Figure 3D-G are based on the M1 scan (Table S1). The (hk0) reciprocal space of the hexagonal TMV structure is shown in Figure S4.

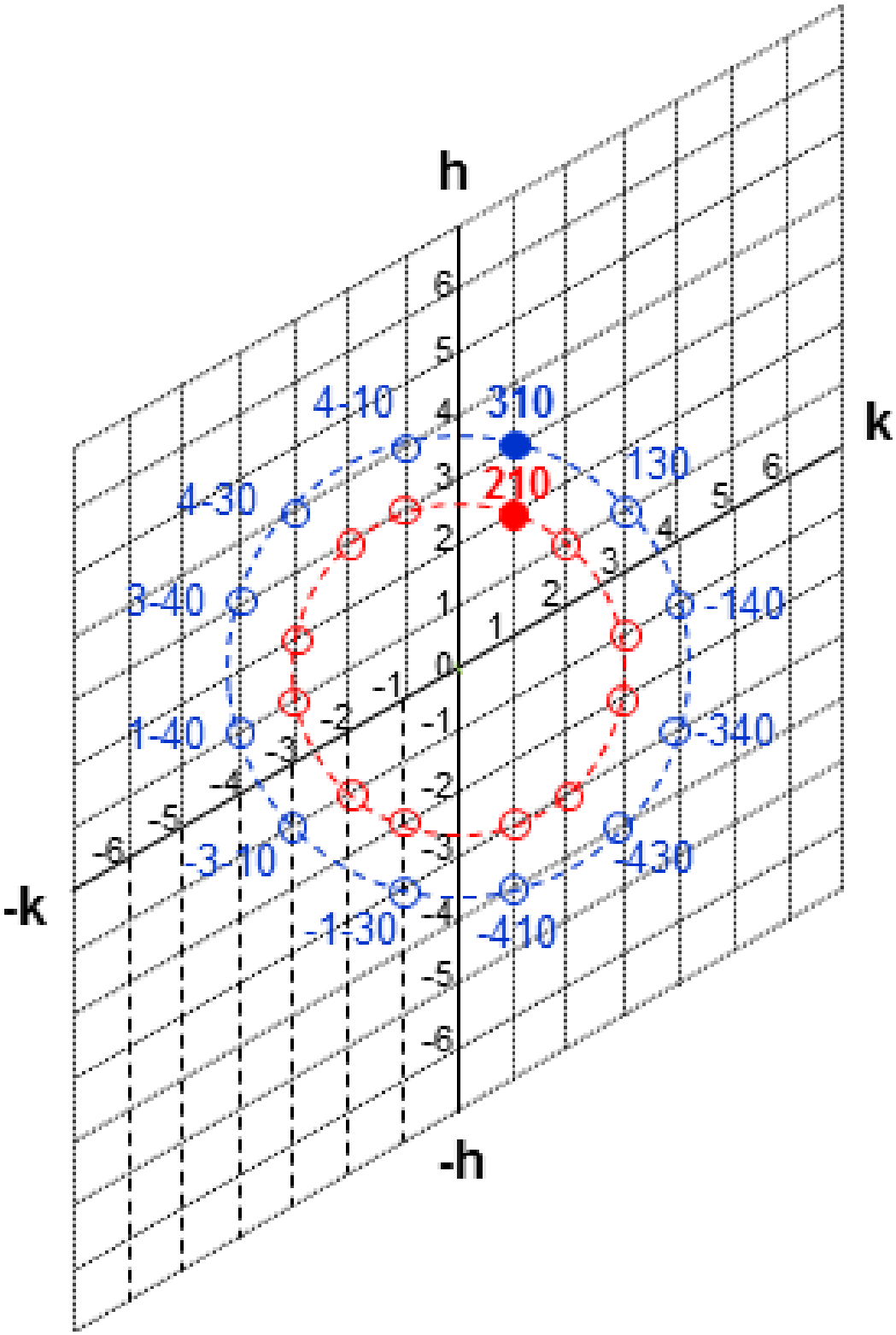

Figure S4 (hk0) reciprocal space for hexagonal TMV structure. The (310) and (210) and symmetry-equivalent reflections are conneceted by dashed circles. The peaks cannot be distinguished for the diffraction geometry used in the present study but could be observed in a microGISAXS experiment[2].

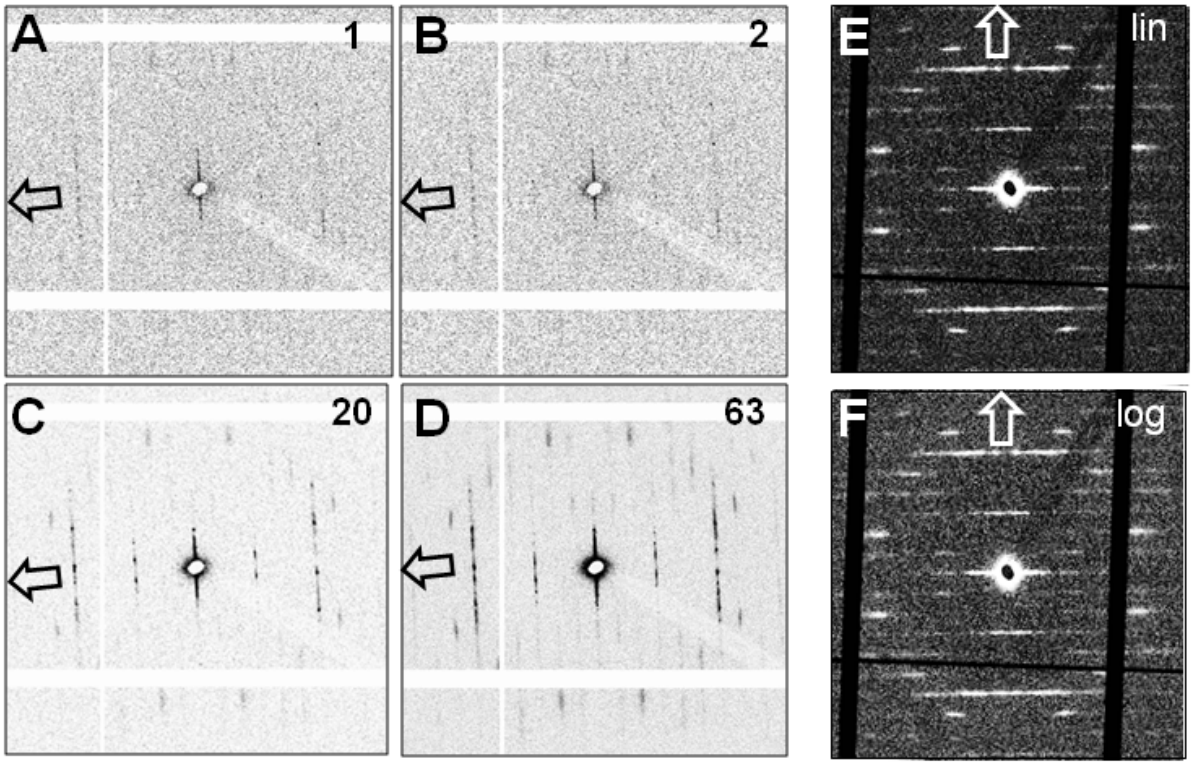

Figure S5 A-D: Central area of patterns from Z_1-zone with the number of patterns averaged indicated top right. The meridional direction is indicated by an open arrow. **E,F**: Grey-scale displays (lin/log) of central area of Figure 5A emphasizing scattering resembling uncorrelated helical TMV nanoparticles. Note that the patterns have been rotated to show the meridional axis in vertical direction.

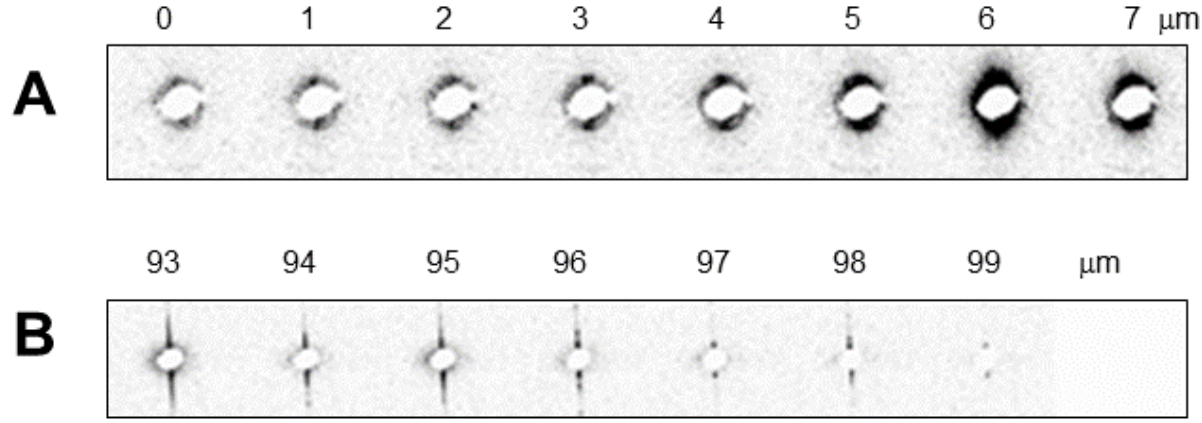

Figure S6 A/B: Scattering around beamstop at the inner boundary (A) and outer boundary zone (B). The positions indicated correspond to the pseudo line-scan from 0 to 101 µm.

The approximate position of the inner boundary interface was determined optically prior to the scan. The starting position of the scan (left upper edges in Figure 3D-G was assumed to be at position 0,0 with y as horizontal (21 positions) and z as vertical (101 positions) axes. We obtained a pseudo line-scan from the patterns of the heat map by averaging of the 21 patterns in each horizontal line. The pseudo line-scan shows the onset of diffuse scattering

around the beamstop at about 5-6 μm (Figure S6A). The position of the outer interface corresponding to the outer boundary zone interface was assumed to correspond to last position (98 μm) of the line-scan revealing an interface streak (Figure S6B).

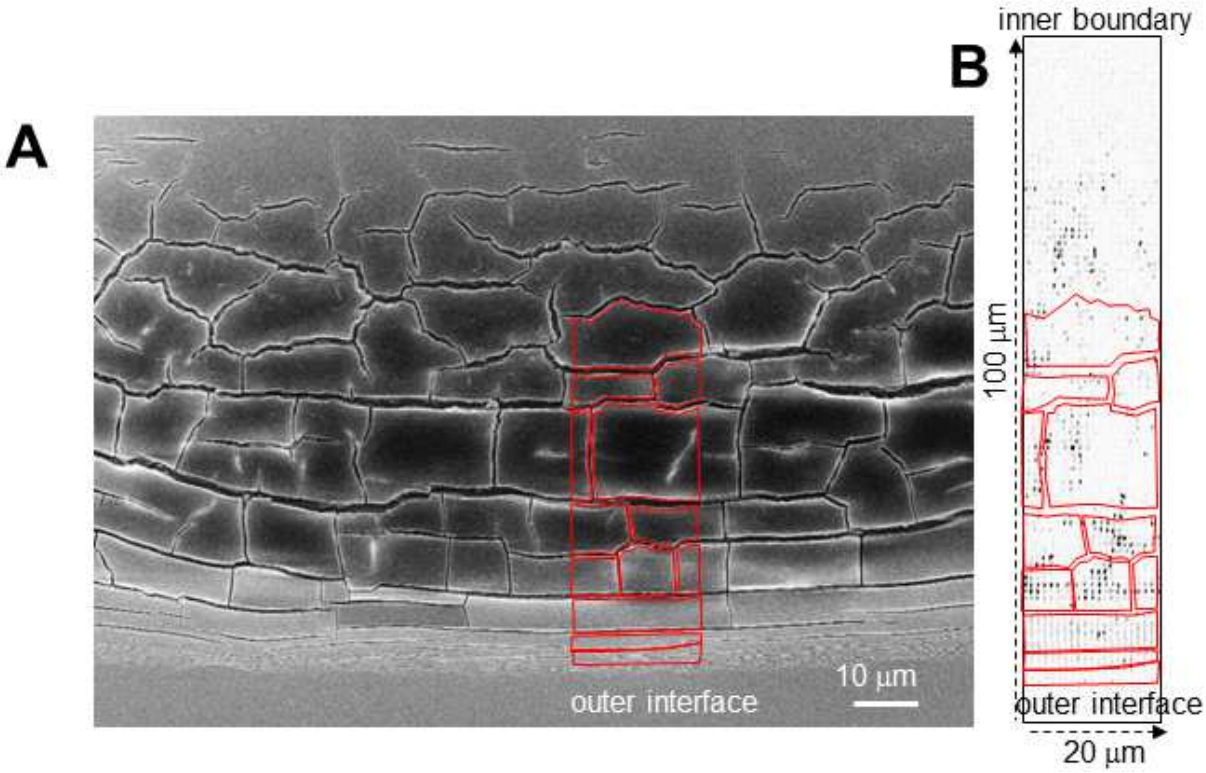

S7A: SEM image of coffee-ring structure (Figure 1E) with part of the block boundaries highlighted in red. **B**: Heat map based on Figure 3F with overlapping contours of the block boundaries. The SEM and heat maps were obtained from the same residue but at different positions.

Dimensional Changes of Capsids during Lateral Compression. A tentative model relating the changes in capsids dimensions to the packing of the threaded nanorods is shown in Figure S8A,B.

Amorphization. Difference SAXS patterns for scan SC2 were calculated by subtracting the 1D intensity profile at T=140 ^{0}C from all other profiles at higher temperatures. The integrated SAXS intensity in each difference pattern was determined in the range $0.32>Q(nm^{-1})<2.60$. The variation of the SAXS intensities with temperature were fitted by a Boltzmann equation (Figure 9B). SEM images of the coffee-ring structure on a Silson Si_3N_4 chip heated 15 min. to 207 ^{o}C in air are shown in Figure S9A,B.

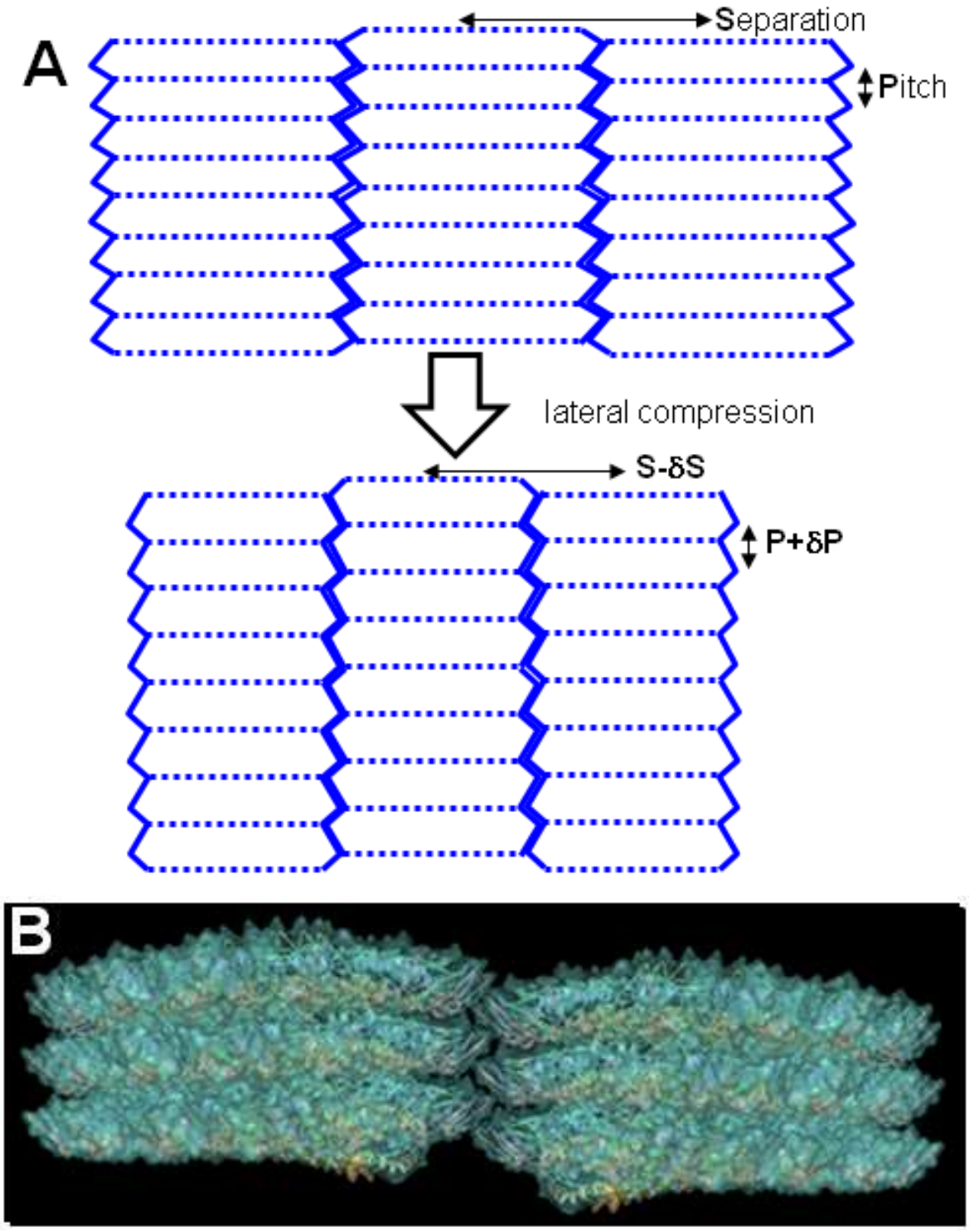

Figure S8 A: Schematic model of axial expansion (P+δP) of threaded nanorods associated with a decrease of their lateral distance S by δS. The about 2% compression and axial expansion has been increased to 20% in the model to enhance its visibility. **B**: Ribbon display model of 3 turns of the TMV X-ray structure (PDB 2TMV)[14] (side-view) created with Protein Workshop[15]. A second group has been added to show the proposed pairing at the level of the grooves and ridges. The surface is shown as partially transparent.

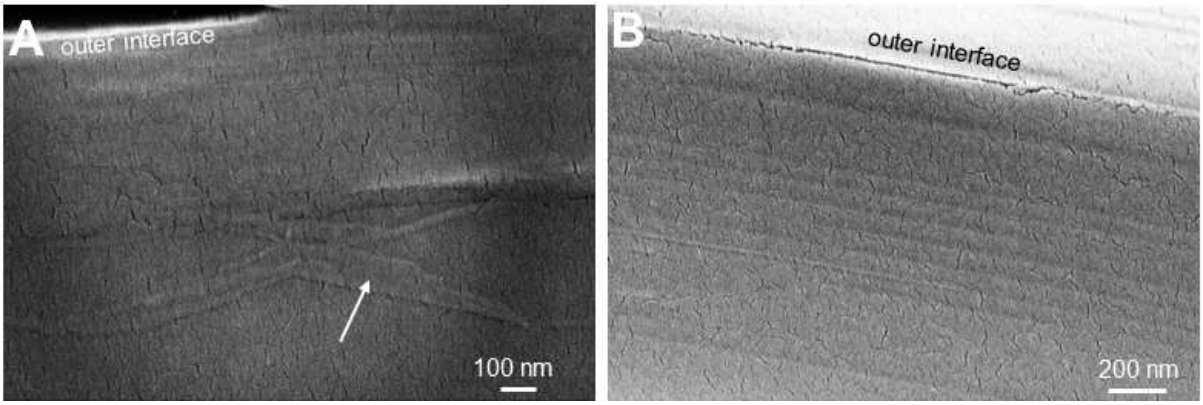

Figure S9 A: SEM image (10kV) of outer boundary zone of coffee-ring structure heated to 207 °C. The network of head-to-tail self-assembled TMV nanorods visible at r.t. (Figure 2D,F) has disappeared. The arrow points at remaining filamentary morphology. **B:** SEM image of outer boundary zone showing steps close to the outer interface (see Figure 2F) but no evidence for lines of TMV nanorods.

Nanocalorimetry experiments. In order to understand the structural change of the TMV structure with increasing temperature, temperature modulated nanocalorimetry was applied. The deposited TMV coffee-ring was subject to a slow heating experiment using an underlying linear heating rate of $10°C \cdot min^{-1}$, overlayed with a heating power modulation of about 20µW using a frequency of 37.5Hz. The slow heating of rate $10°C \cdot min^{-1}$ was chosen to reflect the thermal history of the TMV specimen in the high temperature X-ray nanodiffraction experiments. The response of the sample temperature modulation was recorded as a function of temperature. The calculated change in the sample temperature amplitude together with its phase lag are given in Figure S10. The amplitude and phase lag of the temperature modulation of the TMV coffee-ring is given according to:

$$\Delta T_{Amp} = T_{ref}^{mod} - T_{sample}^{mod}$$

Where T_{ref}^{mod} corresponds the the temperature modulation of the reference (empty sensor) and T_{sample}^{mod} to the temperature modulation of the sample (loaded sensor).

In the initial stage of the heating ramp a drastic increase of the temperature modulation of the sample with respect to the reference can be observed. The maximum modulation response is located at about 100°C marking the end of the evaporation process. This behaviour is typical for water containing specimen, e.g. hydrogels, when measured in an open

system as it is the case in the described experimental setup where a nano-gram sized coffee ring was deposited on a Si_3N_4 membrane with no further encapsulation[16]. In such a case the water evaporation is controlled by the vapour pressure as well as surface-to-volume ratio of the specimens, which in the given case is large[17].

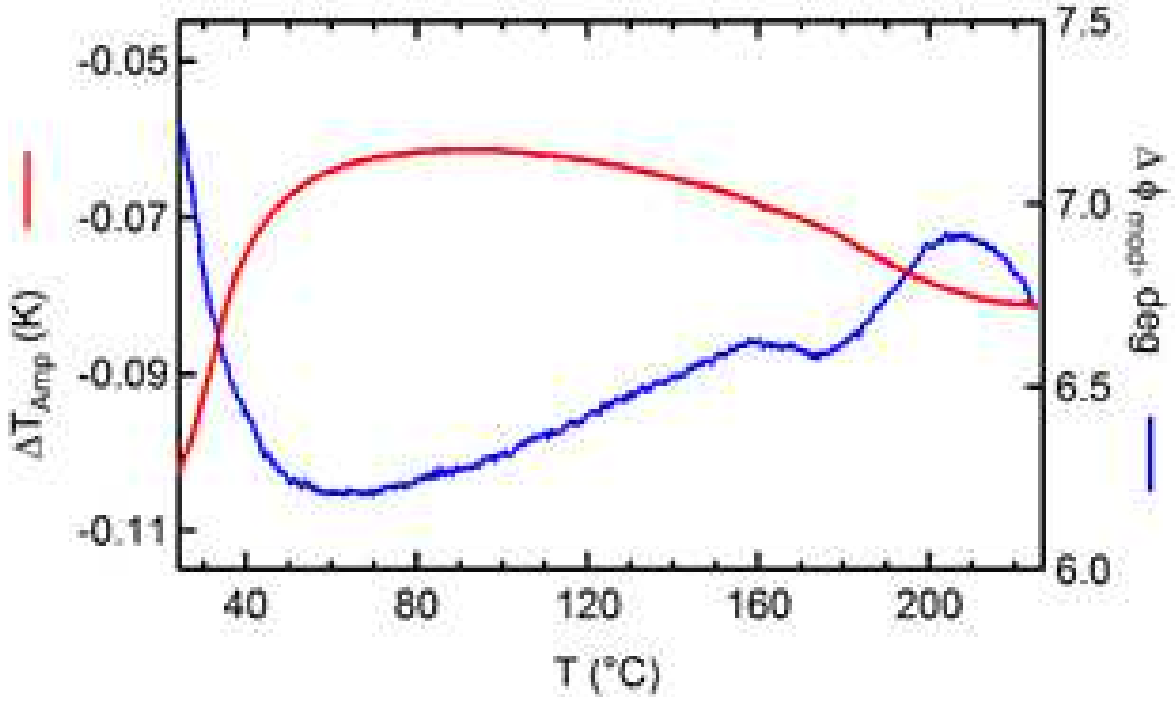

Figure S10 Amplitude and phase lag of the temperature modulation of the TMV coffee ring sample corrected for empty cell signature.

Above 100ºC the sample temperature amplitude decreases again marking an increase in Cp with temperature. At about 160°C the phase signal shows a clear deviation from its baseline indicating the onset of an amorphization process reaching its maximum conversion rate at about 190°C where the response amplitude of the specimen decresses in a stepwise fashion. The amorphization prozess is then finalized at about 210°C being in good aggreement with the X-ray nano-diffraction data shown in Figure 9B.

Temperature Modulated Nanocalorimetry Basics. In the temperature modulated nanocalorimetry a linear temperature program is superimposed with a periodic temperature modulation. The total delivered power to the studied object is given by:

$$P = P_0 + P^{mod}\sin(\omega t)$$

Where P_0 is the power delivered by the linaer heating process, while P^{mod} is the amplitude of the powermodulation applied with a modulation frequency f with $\omega = 2\pi f$.

In the case of nanocalorimetry where a significant ampount of the deployed power is heating the environment in an open system the general balance can be described by:

$$\left(P_0 + P^{mod} sin(\omega t)\right)\Delta t = mc_p \Delta T + Q(T)\Delta t$$

Where m is the mass of the object, c_p its specific heat capacity and T the temperature. $Q(T)$ describes the power of heat losses. In this equation ΔT corresponds to the temperature variation of the object during the time interval Δt. Taking T_0 and T^{mod}, where $T^{mod} << T_0$, and the expression for the heatexchange parameter $Q(T)$,

$$Q(T) = Q(T_0) + Q' T^{mod}$$

the balance can be expressed as:

$$P_0 + P^{mod} sin(\omega t) = mc_p \left(\frac{dT^{mod}}{dt}\right) + Q(T_0) + Q' T^{mod}$$

The conditions for the case of temperature modulated nanocalorimetry are

$(T_0) = P_0$ and $T^{mod} = T_0^{mod} \sin(\omega t - \varphi)$

From this the amplitude T_0^{mod} and phase shift φ of the temperature modulation of the object can be described as:

$T_0^{mod} = \frac{P}{\sqrt{(mc_p\omega)^2 + Q^2}}$ and $\tan\varphi = \frac{mc_p\omega}{Q}$

References

1. A. Asselin and M. Zaitlin, *Virology*, 1978, **88**, 191-193.
2. R. Gebhardt, J. M. Teulon, J. L. Pellequer, M. Burghammer, J. P. Colletier and C. Riekel, *Soft Matter*, 2014, **10**, 5458-5462.
3. C. Schick and V. Mathot, eds., *Fast Scanning Calorimetry*, Springer Nature, 2016.
4. M. Rosenthal, D. Doblas, J. J. Hernandez, Y. I. Odarchenko, M. Burghammer, E. Di Cola, D. Spitzer, A. E. Antipov, L. S. Aldoshin and D. A. Ivanov, *J. Synchr. Rad.*, 2014, **21**, 223-228.

5. R. Graceffa, M. Burghammer, R. Davies, C. Ponchut and C. Riekel, *Appl. Phys. Let.*, 2009, **94**, 062902.
6. X. Shen, C. M. Ho and T. S. Wong, *J. Phys. Chem. B*, 2010, **114**, 5269-5274.
7. A. Accardo, E. D. Fabrizio, T. Limongi, G. Marinaro and C. Riekel, *J. Synchrotron Radiat.*, 2014, **21**, 643-653
8. C. Riekel, E. D. Cola, M. Reynolds, M. Burghammer, M. Rosenthal, D. Doblas and D. A. Ivanov, *Langmuir*, 2014, **31**, 529-534.
9. C. Riekel, M. Burghammer, C. Ferrero, T. G. Dane and M. Rosenthal, *Biomacromolecules*, 2017, **18**, 231-241.
10. J. C. Labiche, O. Mathon, S. Pascarelli, M. A. Newton, G. G. Ferre, C. Curfs, G. Vaughan and A. Homs, *Rev. Sci. Instrum.*, 2007, **78**, 091301.
11. A. Hammersley, *The FIT2D Home Page*, (2009) ESRF, Grenoble.
12. T. N. Blanton, T. C. Huang, H. Toraya, C. R. Hubbard, S. B. Robie, D. Louer, H. E. Goebel, G. Will, R. Gilles and T. Raftery, *Power Diffraction*, 1995, **10**, 91-95.
13. H. P. Klug and L. E. Alexander, *X-ray Diffraction Procedures for Polycrystalline and Amorphous Materials*, 2nd edn., Wiley Interscience, New York, N.Y., 1974.
14. K. Namba, R. Pattanayek and G. Stubbs, *J. Mol. Biol.*, 1989, **208**, 307-325.
15. J. L. Moreland, A. Gramada, O. V. Buzko, Q. Zhang and P. E. Bourne, *BMC Bioinformatics* 2005, **6**, 21.
16. B. Bellich, M. Borgogna, M. Cok and A. Cesaro, *J. Therm. Anal. Calorim.*, 2011, **103**, 81-88.
17. R. J. Seyler, *Thermochimica Acta*, 1976, **17**, 129-136.